

Introduction to HOBIT, a b -Jet Identification Tagger at the CDF Experiment Optimized for Light Higgs Boson Searches

J. Freeman^a, T. Junk^a, M. Kirby^{a,1}, Y. Oksuzian^b, T.J. Phillips^c,
F.D. Snider^a, M. Trovato^e, J. Vizan^f, W.M. Yao^d

^a*Fermi National Accelerator Laboratory, Batavia, IL, 60510, USA*

^b*Univeristy of Virginia, Charlottesville, Virginia, 22906, USA*

^c*Duke University, Durham, North Caronlina, 27708, USA*

^d*Ernest Orlando Lawrence Berkeley National Laboratory,
Berkeley, California, 94720, USA*

^e*Istituto Nazionale di Fisica Nucleare Pisa, Scuola Normale Superiore, I-56127 Pisa, Italy*

^f*Université catholique de Louvain, Louvain la Neuve, B-1348, Belgium*

Abstract

We present the development and validation of the Higgs Optimized b Identification Tagger (HOBIT), a multivariate b -jet identification algorithm optimized for Higgs boson searches at the CDF experiment at the Fermilab Tevatron. At collider experiments, b taggers allow one to distinguish particle jets containing B hadrons from other jets; these algorithms have been used for many years with great success at CDF. HOBIT has been designed specifically for use in searches for light Higgs bosons decaying via $H \rightarrow b\bar{b}$. This fact combined with the extent to which HOBIT synthesizes and extends the best ideas of previous taggers makes HOBIT unique among CDF b -tagging algorithms. Employing feed-forward neural network architectures, HOBIT provides an output value ranging from approximately -1 (“light-jet like”) to 1 (“ b -jet like”); this continuous output value has been tuned to provide maximum sensitivity in light Higgs boson search analyses. When tuned to the equivalent light jet rejection rate, HOBIT tags 54% of b jets in simulated 120 GeV/ c^2 Higgs boson events compared to 39% for SecVtx, the most com-

^{*}FERMILAB-PUB-12-118-PPD

^{*}Corresponding author

Email address: kirby@fnal.gov (M. Kirby)

monly used b tagger at CDF. We present features of the tagger as well as its characterization in the form of b -jet finding efficiencies and false (light-jet) tag rates.

Keywords: b -jet identification, b -tagging, standard model Higgs boson, CDF, Tevatron

1. Introduction

At CDF, the search for a light Higgs boson has been a subject of increasing interest and focus in recent years. While there have been numerous successful b -jet identification algorithms (commonly referred to as “ b taggers”) over the years, most have been intended for use in analyses other than searches for $H \rightarrow b\bar{b}$. Aspects of a given analysis, however, such as the optimal signal-to-background ratio, or the relative rate of non- b jets originating from gluons in the data sample before tagging, can influence whether a tagger is optimal for the analysis in question. Traditional taggers have tended toward a higher purity and lower efficiency than would be ideal for Higgs boson searches given the relatively low cross section of Higgs boson production at Tevatron energies. While this problem has been circumvented somewhat by taking the logical OR of several taggers, a more elegant and flexible solution can be found in the continuous output of a neural network, tunable for each analysis application.

In this paper, we describe the Higgs Optimized b Identification Tagger (HOBIT). The strategy used in developing HOBIT is to build upon the strengths of previous CDF b taggers, address their weaknesses, and construct a new tagger that is highly optimized specifically for finding light Higgs boson decays. HOBIT produces a continuous output variable, allowing efficiency and background rejection to be tuned to meet the requirements of a given search. In the next section, we review some of the general features of b quark decays used by HOBIT to distinguish jets containing B hadrons from jets produced by gluons or light quarks (up, down, or strange). Section 3 then describes some of the previous b -tagging algorithms used by CDF upon which HOBIT is built. We then discuss some features of the CDF detector in Sec. 4, followed by a detailed description of the HOBIT algorithm and training regimen. The performance of HOBIT as characterized by the b -jet tagging efficiency and background rejection rates in data and Monte Carlo (MC) is presented in Sec. 6. We conclude in Sec. 7.

31 **2. Physics of b 's from Higgs Boson Decay**

32 Jets containing high- E_T B hadrons such as are created in a light Higgs
33 boson decay possess several features that distinguish them from jets produced
34 by light quarks or gluons. The most important of these is the relatively long
35 lifetime of a B hadron, augmented in the lab frame by its relativistic boost,
36 which allows it to travel a distance on the order of a millimeter¹. The B
37 hadron's travel across these macroscopic distances results in a displacement
38 between the location of the $p\bar{p}$ collision (the "primary" vertex) and the B
39 hadron decay (the "secondary", or "displaced" vertex). These displacements
40 are resolvable by the CDF tracking system, and in particular by its silicon
41 detector. Almost all information as to whether or not a given jet originates
42 from b -quark production is carried in the tracks reconstructed from detec-
43 tor signals left by the jet's charged particles. Specifically, it is possible to
44 identify the decay of a B hadron through the displacement from the primary
45 vertex of the individual tracks it leaves in the detector, and also through
46 the displacement of a B -hadron decay vertex formed by combining multiple
47 displaced tracks in a fit.

48 Other features also distinguish the b jet from other jets. Due to the large
49 mass of the b quark, the collective invariant mass of the decay products of
50 B hadrons will be larger than those from the decay products of hadrons not
51 containing b quarks. Furthermore, the large relativistic boost typical of a B
52 hadron will result in decay products which tend to be more energetic and
53 collimated within a jet cone than other particles. Finally, particle multiplic-
54 ities tend to be different for jets containing B hadron decays compared to
55 other jets; in particular, muons or electrons appear in approximately 20% of
56 jets containing a B hadron, either directly via semileptonic decay of the B or
57 indirectly through the semileptonic decay of charm hadrons resulting from a
58 B decay.

59 **3. b -Tagging Algorithms**

60 As a tremendous amount of effort has gone into the construction of b
61 taggers at CDF and other experiments [1, 2, 3], we build upon previous
62 experience when constructing HOBIT. In particular, HOBIT explicitly uses

¹This distance is achieved due to the fact that c times the rest frame lifetime of a B^0 (B^\pm , B_s , Λ_b) hadron is 460 μm (501 μm , 441 μm , 367 μm).

63 as inputs the output of the SecVtx algorithm set to its “loose” operating
64 point [4], the output of CDF’s soft muon tagger [5], and inputs to the earlier
65 RomaNN [6, 7] and Bness [8] multivariate taggers. Consequently, it is useful
66 to describe these taggers.

67 3.1. *SecVtx*

68 SecVtx is a displaced vertex tagger and the most commonly used b tagger
69 at CDF. SecVtx only uses tracks which are significantly displaced from the
70 primary vertex, accepted by quality requirements, and within a distance of
71 $\Delta R < 0.4$ of the jet axis. Here, $\Delta R = \sqrt{\Delta\phi^2 + \Delta\eta^2}$, where ϕ is the azimuthal
72 angle of the track around the beam axis, and η is its pseudorapidity defined
73 as $\eta = -\log(\tan(\frac{\theta}{2}))$, with θ the polar angle of the track with respect to
74 the beam axis. With these tracks, SecVtx uses an iterative method to fit a
75 displaced vertex within the jet, where the χ^2 of the vertex fit is employed
76 to guide the process. Assuming that this displacement is due to the long
77 lifetime of the B hadron, the significance of the two-dimensional decay length
78 L_{xy} in the plane perpendicular to the beampipe axis is used to select b -jet
79 candidates. The algorithm is utilized with different track requirements and
80 threshold values in order to achieve different efficiencies and purity rates. In
81 practice, three operating points are used, referred to as “loose”, “tight”, and
82 “ultra-tight”. The loose SecVtx operating point decision is used as an input
83 to both the RomaNN and HOBIT tagger. One drawback of the SecVtx
84 tagger is that it is unable to fit a vertex in every b jet. In the Pythia [9]
85 120 GeV/ c^2 Higgs boson Monte Carlo (MC) whose b jets are used to train
86 HOBIT, SecVtx operating at its “loose” setting fails to find a vertex in 44.3%
87 of these jets.

88 3.2. *Soft Lepton Taggers*

89 Soft lepton taggers [5] (SLT) take a different approach to b tagging.
90 Rather than focusing on tracks within a jet, they select B hadron decays
91 by identifying charged leptons inside a cone around the jet axis. Since the
92 b semileptonic branching ratio is approximately 10% per lepton flavor, this
93 class of tagger is not competitive with SecVtx or the other taggers described
94 below if used alone. However, because a soft lepton tagger does not rely
95 on the presence of displaced tracks or vertices, it has a chance to identify
96 b jets that the other methods cannot. In practice, CDF uses only a soft
97 muon tagger since high-purity electron or τ identification within jets is dif-
98 ficult. HOBIT uses as inputs the number of soft muon tags within a jet

99 as well as the momentum transverse to the jet axis of the muon with the
100 highest-likelihood tag.

101 3.3. *The RomaNN Tagger*

102 The “RomaNN tagger” has been used at CDF in light Higgs boson
103 searches [6, 7] and employs neural network architectures. Neural networks
104 (NNs) can use as many flavor-discriminating observables as is computationally
105 feasible; hence the efficiency of NN taggers is equal to or greater than
106 that of conventional taggers for a given purity. While the SecVtx tagger
107 attempts to find exactly one displaced vertex in a jet, the RomaNN tagger
108 uses a vertexing algorithm that can find multiple vertices, as may be the
109 case when multiple hadrons decay within the same jet cone (for example, in
110 a $B \rightarrow D$ decay). The RomaNN tagger uses several types of NNs: one to
111 distinguish vertices which come from a heavy flavor (B or charm) hadron
112 from false vertices or vertices coming from other hadrons; another to identify
113 unvertexed tracks which come from a heavy flavor hadron; and then another
114 NN which takes as inputs the output of the first NNs along with other inputs,
115 including the loose SecVtx tag status, the number of SLT-identified muons,
116 and the vertex displacement and mass information. Distinct versions of this
117 third NN are trained to separate b jets from light jets, charm jets from light
118 jets, and b jets from charm jets; the outputs of these three flavor-separating
119 NNs are then used to train a final NN whose output is the RomaNN discrim-
120 ination variable. The RomaNN tagger not only has superior performance
121 to that of SecVtx at equivalent purities (see Fig. 5), but also allows for an
122 “ultra-loose” operating point yielding greater efficiency, particularly useful
123 in light Higgs boson searches.

124 However, the RomaNN tagger is not guaranteed to fit a vertex or to
125 have sufficient input information to reliably tag a jet. In the event that the
126 RomaNN tagger fails to receive sufficient information from its inputs, it is
127 unable to assign an output value to that jet. This is the case with 20.6% of
128 the b jets in the aforementioned light Higgs boson MC sample. Regardless,
129 due to the usefulness of the RomaNN inputs, a majority of them are employed
130 as inputs into the HOBIT tagger, which allows HOBIT to take advantage of
131 the same extensive vertex information that the RomaNN tagger uses.

132 3.4. *The Bness Tagger*

133 While the RomaNN tagger focuses on the vertices it finds within a jet, in
134 the event that it is unable to fit any vertices, it is unable to distinguish b jets

135 from light jets. However, a significant proportion of b jets (approximately
 136 20% in Higgs boson candidate events) do not contain a sufficient number
 137 of well-reconstructed tracks to allow for a vertex fit in the RomaNN tagger.
 138 The Bness tagger [8] uses not only vertex information within a jet, but also
 139 the properties of individual tracks to determine whether a jet is b -like. (The
 140 RomaNN tagger only examines individual tracks based on their proximity
 141 to a displaced vertex). To evaluate the information from individual tracks,
 142 the Bness tagger utilizes an NN which is applied to all tracks passing loose
 143 requirements, and which takes positional (e.g., impact parameter) and kine-
 144 matic (e.g., p_T) information on a track to determine whether it appears to
 145 have come from the decay of a B hadron. The Bness tagger is therefore able
 146 to extract information from all but a few percent of B jets, and can achieve
 147 a very high efficiency for a reasonable level of purity. This robust property
 148 of the tagger makes it useful for analyses where efficiency is critical, as is
 149 the case with light Higgs boson analyses or even searches for hadronic de-
 150 cays of heavy gauge bosons (see Ref. [10] for more details). A track-by-track
 151 NN very similar to that employed by the Bness tagger is used to evaluate
 152 tracks in HOBIT; this will be described in Section 5. One drawback of the
 153 Bness tagger is that, like SecVtx and unlike RomaNN, it is only able to fit
 154 one vertex per jet. Additionally, it uses fewer vertex-based inputs than the
 155 RomaNN tagger, and therefore only its track-by-track algorithm is used in
 156 HOBIT.

157 4. The CDF Detector

158 The CDF II detector is described in detail elsewhere [11]. The detector is
 159 cylindrically symmetric around the proton beam line² with tracking systems
 160 that sit within a superconducting solenoid which produces a 1.4 T magnetic
 161 field aligned coaxially with the $p\bar{p}$ beams. A set of calorimeters and muon
 162 detectors, to be described later, surround the tracking systems and solenoid.

163 The outermost tracking system, the Central Outer Tracker (COT), is a
 164 3.1 m long open cell drift chamber which performs up to 96 track position
 165 measurements in the region between 0.40 and 1.37 m from the beam axis,

²The proton beam direction is defined as the positive z direction. The rectangular
 coordinates x and y point radially outward and vertically upward from the Tevatron ring,
 respectively. Transverse energy, and transverse momentum are defined as $E_T = E \sin \theta$, and
 $p_T = p \sin \theta$, respectively, θ having been defined in Sec. 3

166 providing coverage in the pseudorapidity region $|\eta| \leq 1.0$ [12]. Sense wires
167 are arranged in eight alternating axial and $\pm 2^\circ$ stereo “superlayers” with 12
168 wires each. The position resolution of a single drift time measurement is
169 about $140 \mu\text{m}$.

170 Charged-particle trajectories are found first as a series of approximate line
171 segments in the individual axial superlayers. Two complementary algorithms
172 associate segments lying on a common circle, and the results are merged
173 to form a final set of axial tracks. Track segments in stereo superlayers
174 are associated with the axial track segments to reconstruct tracks in three
175 dimensions.

176 A five layer double-sided silicon microstrip detector (SVX) covers the
177 region between 2.5 to 11 cm from the beam axis. Three separate SVX barrel
178 modules along the beam line together cover a length of 96 cm, approximately
179 90% of the luminous beam interaction region. Three of the five layers combine
180 an r - ϕ measurement on one side and a 90° stereo measurement on the other,
181 and the remaining two layers combine an r - ϕ measurement with small angle
182 stereo at $\pm 1.2^\circ$. The typical silicon hit resolution is $11 \mu\text{m}$. Additional
183 Intermediate Silicon Layers (ISL) at radii between 19 and 30 cm from the
184 beam line in the central region link tracks in the COT to hits in the SVX.

185 Silicon hit information is added to COT tracks using a progressive “outside-
186 in” tracking algorithm in which COT tracks are extrapolated into the silicon
187 detector, associated silicon hits are found, and the track is refit with the
188 added information of the silicon measurements. The initial track parameters
189 provide a width for a search road in a given layer. Then, for each candidate
190 hit in that layer, the track is refit and used to define the search road into the
191 next layer. This stepwise addition of precision SVX information at each layer
192 progressively reduces the size of the search road, while also accounting for the
193 additional uncertainty due to multiple scattering in each layer. The search
194 uses all candidate hits in each layer to generate a small tree of final track
195 candidates, from which the tracks with the best χ^2 are selected. The effi-
196 ciency for associating at least three silicon hits with an isolated COT track is
197 $91 \pm 1\%$. The extrapolated impact parameter resolution for high-momentum
198 outside-in tracks is much smaller than for COT-only tracks: $40 \mu\text{m}$, domi-
199 nated by a $30 \mu\text{m}$ uncertainty in the beam position.

200 Outside the tracking systems and the solenoid, segmented calorimeters
201 with projective geometry are used to reconstruct electromagnetic (EM) show-
202 ers and jets. The EM and hadronic calorimeters are lead-scintillator and iron-
203 scintillator sampling devices, respectively. The central and plug calorimeters

204 are segmented into towers, each covering a small range of pseudorapidity and
 205 azimuth, and in full cover the entire 2π in azimuth and the pseudorapidity
 206 regions of $|\eta| < 1.1$ and $1.1 < |\eta| < 3.6$ respectively. The transverse energy, E_T ,
 207 where the polar angle is calculated using the measured z position of the event
 208 vertex, is measured in each calorimeter tower. Proportional chambers and
 209 scintillation detectors arranged in strips measure the transverse profile of EM
 210 showers at a depth corresponding to the shower maximum.

211 High-momentum jets, photons, and electrons leave isolated energy de-
 212 posits in contiguous groups of calorimeter towers which can be summed to-
 213 gether into an energy “cluster”. Electrons are identified in the central EM
 214 calorimeter as isolated, mostly electromagnetic clusters that also match with
 215 a track in the pseudorapidity range $|\eta| < 1.1$. The electron transverse energy
 216 is reconstructed from the measured energy in the electromagnetic cluster
 217 with precision $\sigma(E_T)/E_T = 13.5\%/\sqrt{E_T(\text{GeV})} \oplus 2\%$, where the \oplus symbol
 218 denotes addition in quadrature. Jets are identified as a group of electro-
 219 magnetic and hadronic calorimeter clusters using the JETCLU algorithm [13]
 220 with a cone size of $\Delta R = 0.4$. Jet energies are corrected for calorimeter non-
 221 linearity, losses in the gaps between towers, multiple primary interactions, the
 222 underlying event, and out-of-cone losses [14]. The jet energy resolution is
 223 approximately $\sigma_{E_T} = 1.0 \text{ GeV} + 0.1 \times E_T$.

224 Directly outside of the calorimeter, four-layer stacks of planar drift cham-
 225 bers detect muons with $p_T > 1.4 \text{ GeV}/c$ that traverse the five absorption
 226 lengths of the calorimeter. Farther out, behind an additional 60 cm of steel,
 227 four layers of drift chambers detect muons with $p_T > 2.0 \text{ GeV}/c$. The two
 228 systems both cover the region $|\eta| \leq 0.6$, though they have different struc-
 229 tures, and therefore places where the geometrical coverage does not overlap.
 230 Muons in the region $0.6 \leq |\eta| \leq 1.0$ pass through at least four drift layers
 231 arranged in a conic section outside of the central calorimeter. Muons are
 232 identified as isolated tracks in the COT that extrapolate to track segments
 233 in one of the four-layer stacks.

234 5. The HOBIT Tagger

235 The HOBIT tagger is similar to other multivariate b -tagging algorithms
 236 previously used at CDF, such as the RomaNN and Bness taggers. All of
 237 these taggers attempt to make maximal use of the available information in
 238 b jets, and construct a continuous discriminating variable. HOBIT improves

239 upon these earlier taggers, however, by addressing specific weaknesses of each
240 and optimizing for light Higgs boson searches.

241 5.1. The architecture

242 HOBIT is constructed as a feed-forward multilayer perceptron neural net-
243 work implemented using the TMVA package for Root [15]. It consists of two
244 hidden layers of 25 and 26 nodes, there being 25 inputs to the tagger, and a
245 hyperbolic tangent activation function. Five hundred cycles were used in the
246 training. The training regimen used b jets in Pythia [9] 120 GeV/ c^2 Higgs bo-
247 son Monte Carlo (MC) and light jets from Alpgen-generated Pythia W +jets
248 MC. Charm jets were not considered during training due to preliminary stud-
249 ies which indicated a relative insensitivity of light Higgs boson searches to
250 charm jet contamination. Here, “ b jet” denotes a jet with a B hadron within
251 a cone of $\Delta R < 0.4$ of the jet axis, while a “charm jet” contains a charm
252 hadron but no B hadrons within this cone and a “light jet” contains neither
253 B hadrons nor charm hadrons within this cone. Jets were required to have
254 an $E_T > 15$ GeV, $|\eta| < 2$, and at least one track for use in the track-by-track
255 NN described in Sec. 5.3.

256 The 25 inputs to the tagger are a combination of RomaNN and Bness
257 inputs, albeit with some exceptions, additions and modifications. Fourteen
258 of these inputs are also inputs to the RomaNN tagger. A further ten inputs
259 to HOBIT are the ten highest track-by-track NN discriminant output values
260 of tracks in the jet cone. In the event that there are fewer than ten tracks
261 in a jet, the value of the remaining track-by-track NN inputs are set to -
262 1 as this is the light-jet-like value of the NN output. The number of tracks
263 which pass the track-by-track NN selection criteria is found to have additional
264 discriminating power and is also used as an input to HOBIT. Track selections
265 differ between tracks used for RomaNN inputs and tracks evaluated with
266 the track-by-track NN. Tracks used for RomaNN inputs must have $p_T > 1$
267 GeV/ c and be within $\Delta R < 0.4$ of the jet axis (the same selection used
268 in the published RomaNN tagger), while tracks used by the track-by-track
269 NN inputs had a looser requirement of $p_T > 0.5$ GeV/ c and a distance of
270 $\Delta R < 0.7$ from the jet axis (the original requirement was $\Delta R < 0.4$). Other
271 selection cuts were considered, but none resulted in an improvement in the
272 performance of HOBIT. Note that one of the RomaNN inputs used (also used
273 in the Bness tagger) is the E_T of the jet itself. The various HOBIT inputs
274 are correlated with E_T , so the E_T provides additional useful information to

275 HOBIT. We prevent kinematic biasing of HOBIT by weighting the light jet
276 training sample to have the same E_T distribution as the b -jet training sample.

277 As previously mentioned, one potential weakness of the RomaNN tagger
278 is its inability to produce a useable output when there is insufficient input
279 information. This requirement of “RomaNN taggability” can be a liability
280 when very high b -jet tagging efficiency is sought. In the MC sample used to
281 train the HOBIT tagger, 21% of b jets fail to be RomaNN taggable, versus
282 30% of light jets. The track-by-track NN in HOBIT compensates for this
283 shortfall of RomaNN. While jets in HOBIT are required to have at least one
284 track with an evaluated track-by-track NN output, only 3.0% of b jets and
285 2.1% of light jets in the MC fail this requirement, indicating a very efficient
286 taggability requirement.

287 The full list of inputs to HOBIT ranked by importance after TMVA’s
288 training is provided in Table 1. Here, “importance” refers to the sum of
289 the squares of the weights connecting a given input to the nodes of the first
290 hidden layer of HOBIT. Distributions of the inputs to HOBIT are shown in
291 Fig. 1. A description of these inputs is given below.

292 5.2. The RomaNN inputs

293 RomaNN inputs used in HOBIT consist of observables built using tracks
294 and vertices found to be “heavy-flavor-like” (HF-like) according to its NNs.
295 No modifications were made to the RomaNN inputs compared to the pub-
296 lished tagger. These inputs include:

- 297 • The invariant mass, pseudo- $c\tau$, 3-d displacement and 3-d displacement
298 significance of the most HF-like vertex.
- 299 • The number of tracks both in HF-like vertices and standalone HF-
300 like tracks associated to a displaced vertex, as well as their combined
301 invariant mass, and the ratio of the scalar sum of the p_T ’s of these
302 tracks to the scalar sum of the p_T ’s of all tracks in the jet.
- 303 • The loose SecVtx tag status, as well as the mass of the tracks used in
304 the loose SecVtx vertex fit.

305 5.3. Bness inputs: the track-by-track NN

306 As mentioned above, the ten highest evaluated track-by-track NN outputs
307 for tracks in a jet serve as inputs to HOBIT. Therefore, this section concerns
308 the track-by-track NN itself. The input variables to the track-by-track NN

309 are the same for HOBIT as were used in the track-by-track NN of the orig-
 310 inal Bness tagger. However, the track-by-track Bness NN was retrained to
 311 create the HOBIT track-by-track NN. This was done not only because the
 312 cone requirement on the tracks was loosened but also because we wished to
 313 optimize the track-by-track NN for light Higgs boson searches. Hence, while
 314 the original Bness track-by-track NN was trained using $ZZ \rightarrow 4$ jets MC,
 315 the HOBIT track-by-track NN was trained using the same MC as was used
 316 to train the overall HOBIT tagger. Since the track-by-track NN operates
 317 at the level of individual tracks, we impose an additional requirement on
 318 b -jet tracks for the purposes of training by demanding that they be within
 319 $\Delta R < 0.05$ of the actual charged particles resulting from a B hadron decay
 320 in the MC. The track-by-track NN employed the same basic framework for
 321 training as that used for HOBIT itself (training cycles, inner layer structure,
 322 etc.).

323 Some of the inputs to the track-by-track NN take advantage of the fact
 324 that tracks from B hadron decays are displaced from the primary vertex.
 325 These inputs include the impact parameter, the distance along the z-axis be-
 326 tween the track and the primary vertex, and the significance of each. Kine-
 327 matic inputs such as the p_T , rapidity, and track momentum perpendicular
 328 to the jet axis (p_{perp}) exploit the greater collimation of B tracks due to the
 329 large boost of the hadron. Finally, the jet E_T is an input to the track-by-
 330 track NN, because the previously mentioned inputs are correlated with jet
 331 E_T . Tracks from light jets are weighted in training such that the jets which
 332 contain them have the same E_T distribution as the b jets; this is done so
 333 as to avoid kinematic biasing in the track-by-track NN. Distributions of the
 334 track-by-track NN inputs are shown in Fig. 2. Not shown are the jet E_T
 335 distributions, which are identical by construction.

336 5.4. HOBIT Performance

337 The output HOBIT distributions for b -jets and light-jets from an inde-
 338 pendent but identically generated MC sample as was used to train the dis-
 339 criminator are shown in Fig. 3. In Fig. 4, the b -jet efficiencies and the light
 340 jet efficiencies (“mistag rates”) as a function of jet E_T and η are shown for
 341 two HOBIT operating points – a requirement of a HOBIT output > 0.72
 342 (“loose”) and a requirement of a HOBIT output > 0.98 (“tight”). At higher
 343 η , where tracking coverage is more sparse and less information is available,
 344 the b -tagging efficiency drops, as would be expected. Interestingly, the mistag
 345 rate increases in the case of the loose tag and drops in the case of the tight

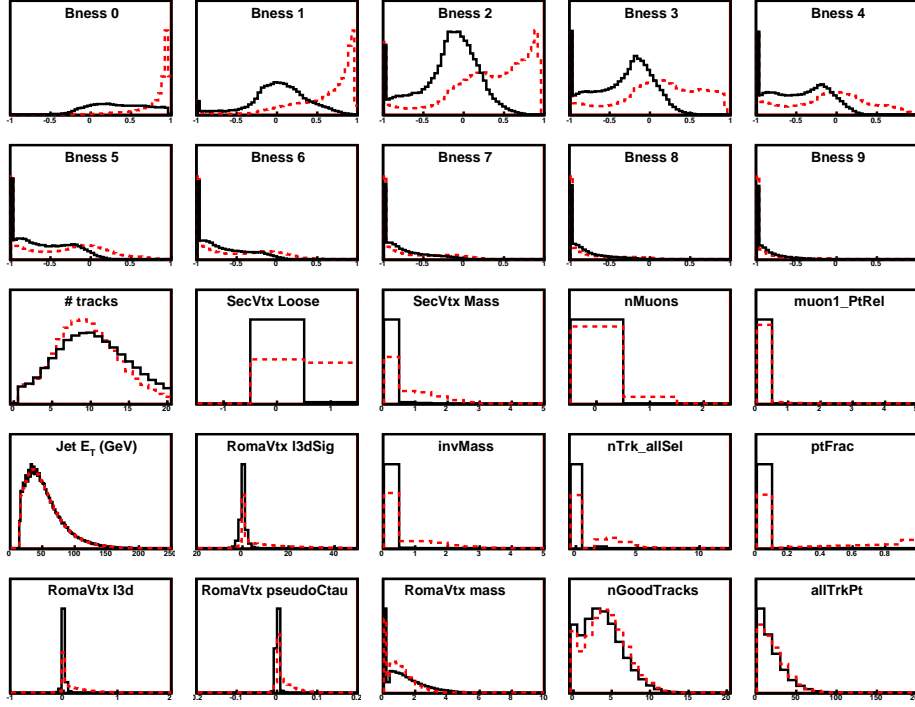


Figure 1: Inputs to HOBIT. The solid histogram is for light quark jets and the dashed (colored) histogram is for b jets. Taken from MC, the distributions are normalized to one another. Left to right, top to bottom: the Bness value for the 10 highest Bness tracks; the number of Bness-selected tracks; the loose SecVtx tag status and the mass of its fitted vertex; the number of SLT-tagged muons and the momentum transverse to the jet axis of the most SLT-favored muon; jet E_T ; the 3-d displacement significance of the most HF-like vertex in RomaNN; the invariant mass, number, and fraction of total track p_T of HF-like tracks; the 3-d displacement, pseudo- $c\tau$ and invariant mass of the most HF-like vertex; the number of RomaNN-selected tracks and their total p_T .

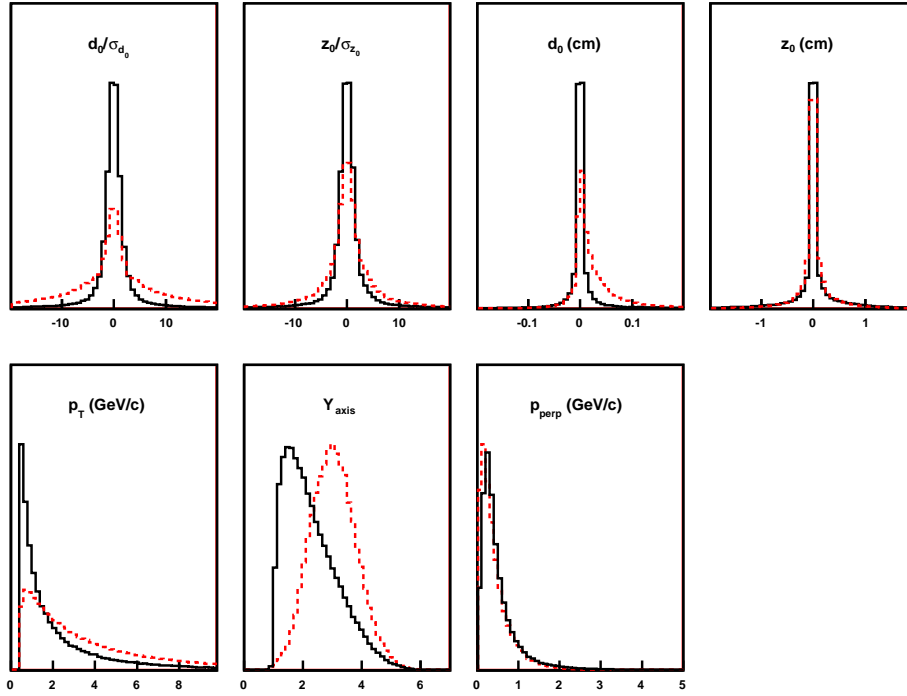


Figure 2: Inputs to track-by-track NN. The solid histogram is for tracks in light quark jets and the dashed (colored) histogram is for tracks in b jets; taken from MC, the distributions are normalized to one another. Not shown is the jet E_T , identical between the two distributions by construction. Left-to-right, top-to-bottom: significance of the impact parameter and Δz between the track and the primary vertex; the values of the impact parameter and Δz ; the p_T of the track with respect to the beam axis; and the track's rapidity and p_T with respect to the jet axis.

346 tag, demonstrating the higher impact of incorrectly identified tracks when
 347 using a loose tagging requirement. In general, the efficiency increases with
 348 increasing jet E_T due to the greater displacement of the B hadron. Similarly,
 349 the light jet efficiency increases, at least in part due to the higher rapidity
 350 and p_T of tracks in high- E_T jets.

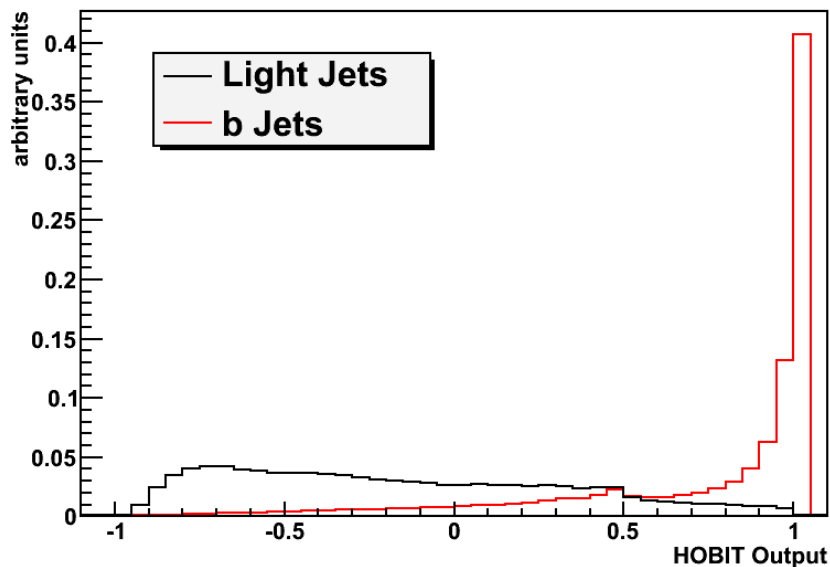


Figure 3: HOBIT outputs. The output is trained so that 1 is b jet-like and -1 is targeted to be light jet-like. The black histogram is for light quark jets and the colored histogram is for b jets. Taken from MC, the distributions are normalized to one another.

351 The performance of a tagger is best evaluated by comparing its purity to
 352 tagging efficiency at given operating points. We compare HOBIT's purity
 353 versus efficiency curve to the curves of the Bness and RomaNN taggers and
 354 to the purity versus efficiency performance of SecVtx at both its tight and
 355 loose operating points (Fig. 5). Here, purity refers to the fraction of light-jets
 356 in W +jets MC which are not tagged as b -jets, and efficiency refers to the
 357 fraction of b jets in light Higgs boson MC which are tagged. When evaluating
 358 tag efficiencies, the jets in both the numerator and denominator are required
 359 to have $E_T > 15$ GeV and $|\eta| < 2$, the same E_T and η requirements as
 360 were placed on the jets in the training of HOBIT. Fig. 5 shows that for a

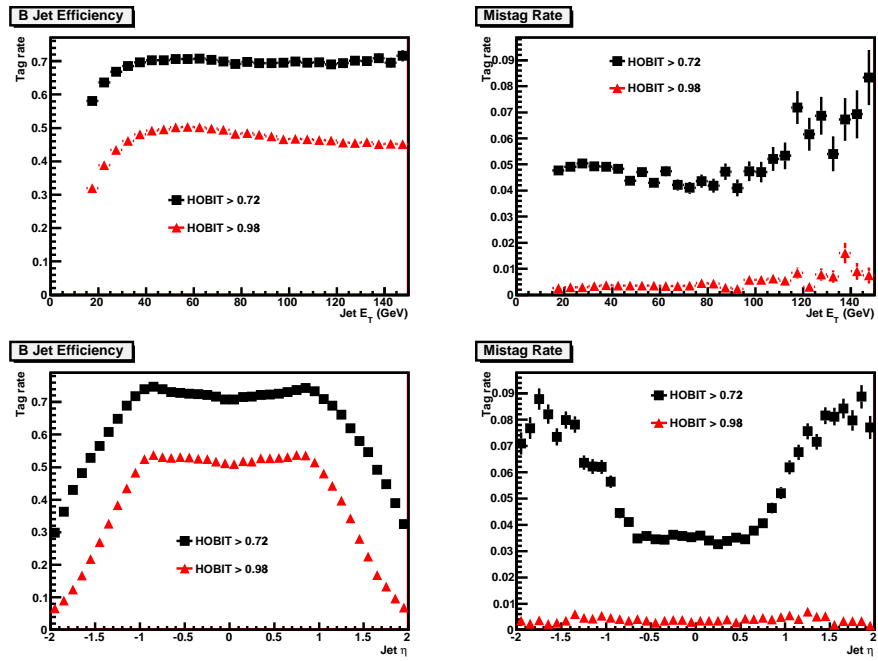


Figure 4: The b -jet and light-jet efficiencies in MC before SF corrections as a function of η and E_T . The black triangles are for the looser operating point and the colored triangles are for the tighter operating point.

361 given purity level, improvement in the absolute efficiency due to HOBIT is
362 approximately 10% over the Bness and RomaNN taggers, and approximately
363 15% over the SecVtx tagger.

364 We investigated how much of the improvement in HOBIT over earlier
365 taggers is due to the optimization on jets that specifically originated from
366 Higgs boson decays. To study this, we trained NN taggers that take the same
367 inputs as Bness and RomaNN using W+jets and light Higgs boson MC, then
368 compared the purity versus efficiency curve with those of the original Bness
369 and RomaNN taggers, which were trained using ZZ MC and Z+jets MC,
370 respectively. The results can be seen in Figs. 6 and 7. In the case of the
371 RomaNN comparison, not only is our retrained RomaNN tagger compared
372 with the original RomaNN result, but also with RomaNN's b versus light jet
373 separator. This is because the architecture of RomaNN consisted of three
374 different NN separators (b versus light, b versus charm, light versus charm)
375 which fed into the final RomaNN separator. As we retrained using light and
376 b jets, the comparison of the Higgs-optimized version of the RomaNN tagger
377 with the original b versus light separator makes for a more fair comparison.
378 In both the Bness and RomaNN cases, the improvement in absolute efficiency
379 is approximately 2%.

380 6. Efficiency and Mistag Scale Factors

381 In order to be used in a physics analysis, the performance of the HOBIT b
382 tagger must be calibrated. Historically, MC modeling of b -tag efficiencies and
383 mistag rates has not been sufficient to use the uncorrected predictions of the
384 MC. Instead, we use various techniques to measure the b -tagging efficiency
385 and the mistag rate using CDF data. Examples of such techniques applied
386 to the SecVtx algorithm are using jets containing electrons (therefore HF-
387 enriched) for measuring the b -tagging efficiency [16], and using the rate at
388 which jets have a displaced vertex reconstructed behind the primary vertex
389 ("negative tags") to estimate mistags [17]. For the tight SecVtx tagger,
390 the b -tag efficiency is found to be well predicted by the MC up to a scale
391 factor (SF), where $SF = 0.96 \pm 0.05$ for the full CDF dataset. In order to
392 utilize HOBIT to predict yields in data from MC simulation, a similar level
393 of uncertainty in HOBIT's SF to that of SecVtx's SF is needed for each
394 operating point.

395 An important difference between SecVtx and HOBIT is the absence of
396 negative tags in HOBIT, meaning the SecVtx mistag calculation technique

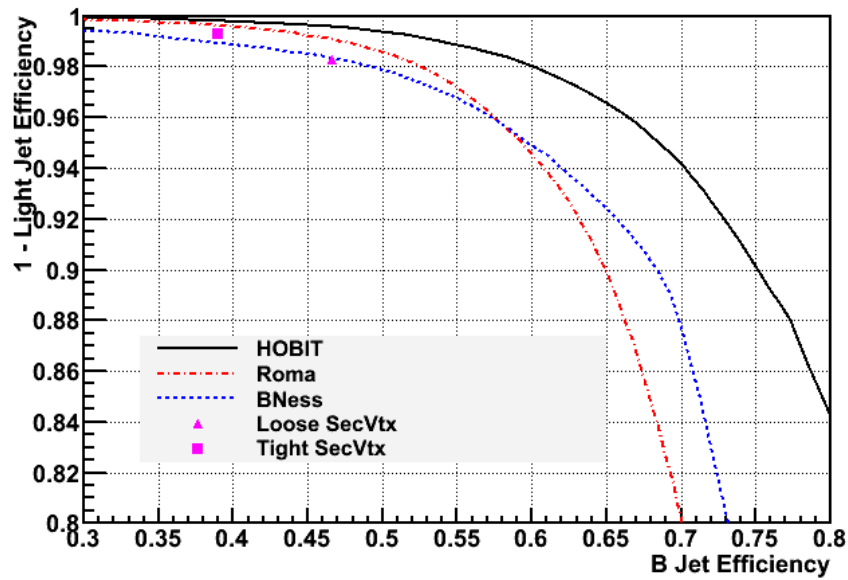


Figure 5: A comparison of the purity-efficiency tradeoffs for HOBIT versus RomaNN, Bness, and SecVtx loose and tight. A significant improvement over prior multivariate taggers is seen.

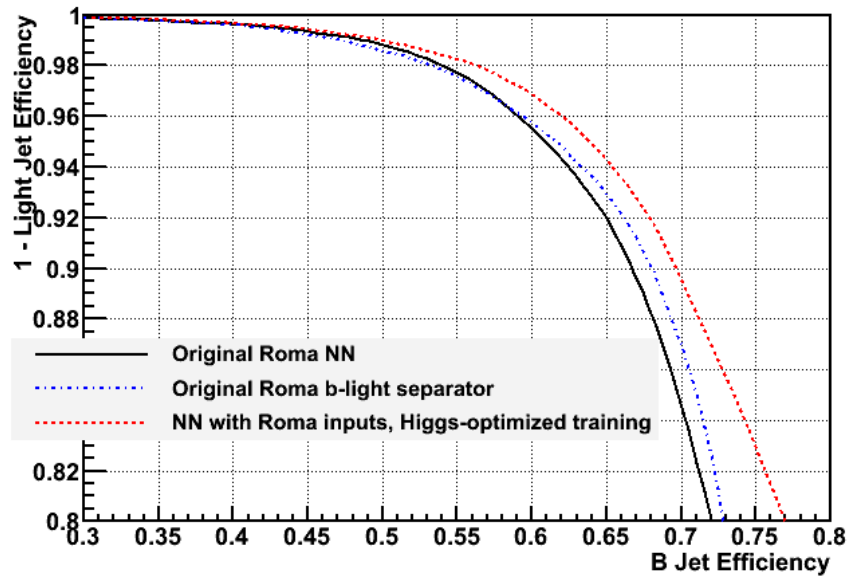


Figure 6: A comparison of the purity-efficiency tradeoffs for the original RomaNN tagger (as well as its *b*-light separator) and our version of the Higgs-optimized RomaNN tagger.

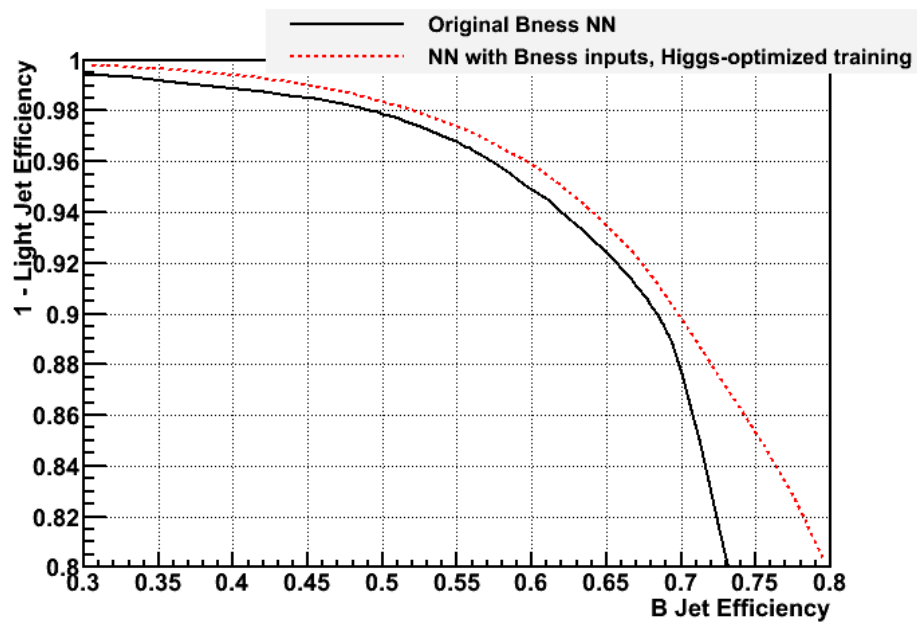


Figure 7: A comparison of the purity-efficiency tradeoffs for the original Bness tagger and our version of the Higgs-optimized Bness tagger.

397 cannot be applied. Instead, we use two new techniques described below
 398 for calibrating b -tag SFs and providing mistag rates: the “ $t\bar{t}$ cross section
 399 method”, and the “electron conversion method”.

400 *6.1. Scale factors using the $t\bar{t}$ cross section method*

401 The $t\bar{t}$ cross section method seeks to calibrate the predicted b -tagging
 402 efficiency and the mistag rate in MC to match those measured in data using
 403 $t\bar{t}$ candidate events in a $W+3$ -or-more-jets sample under the assumption
 404 that the $t\bar{t}$ cross section is known. The method is based upon a previous
 405 analysis [18] that simultaneously measured the SecVtx b -tag SFs and the $t\bar{t}$
 406 cross section. In that measurement, the rates of singly and double tagged
 407 events provide a constraint which allows the measurement of two unknowns.
 408 A two-dimensional fit was performed to maximize the likelihood of observing
 409 the data counts as functions of the SecVtx b -tag SF and the $t\bar{t}$ cross section.

410 This method has been repurposed such that the $t\bar{t}$ cross section is now an
 411 input assumption, allowing for the calibration of the HOBIT b -tag efficiency
 412 and the HOBIT mistag rate. We parameterize the resulting tag rate in the
 413 MC samples as a 5-dimensional matrix, where each element is the measured
 414 rate within a bin of the following five variables: jet E_T , jet η , the number
 415 of tracks in the jet, the number of primary vertices in the event, and the
 416 z location of the primary vertex from which the jet is calculated to have
 417 originated. The matrix is similar to the SecVtx mistag matrix [17], although
 418 of a lower dimension; the variables it has in common with the SecVtx mistag
 419 matrix have the same binning between the two matrices. For eight different
 420 HOBIT operating points, separate matrices are constructed for b , charm, and
 421 light jets.

422 The $W+3$ -or-more-jets sample has an insufficient number of mistags to
 423 calibrate the mistag SF, so we add a $W+1$ jet sample, which before b -tagging
 424 requirements is almost pure W +light flavor (LF) events. After b tagging,
 425 the $W+1$ jet sample consists of comparably sized $Wb\bar{b}$, $Wc\bar{c}$, Wcj , and
 426 mistagged W +LF events. The background predictions [4] involve scaling
 427 the total W +jets rate to data and subtracting off the non- W +jets compo-
 428 nents. The prediction of the W +HF component of W +jets relies on the HF
 429 K -factor. This scaling adjusts leading-order theoretical predictions of the
 430 fraction of HF in W +jets events to account for higher-order corrections. We
 431 find that the $W+1$ -jet data provides an independent handle on the mistag
 432 SF while the b -tag SF is constrained by the events with three or more jets.

433 However, the dependence on the HF K -factor introduces a systematic un-
 434 certainty that strongly affects the mistag SF. For low values of the HOBIT
 435 cut, the mistag rate is relatively high, and the relative contribution to the
 436 tagged $W+1$ -jet sample from $W+HF$ events is lower. This translates to a
 437 systematic uncertainty on the mistag SF due to the uncertainty on the HF
 438 K -factor that is lower at low HOBIT output values than at high HOBIT
 439 output values.

440 The maximum of the 2-d likelihood for the b -tag SF and the mistag SF is
 441 calculated given the observed data and fixed values of the HF K -factor, the
 442 $t\bar{t}$ cross section, and the minimum HOBIT output value. The dependence
 443 on the HF K -factor and the $t\bar{t}$ cross section are then taken as sources of
 444 systematic uncertainty. We assume $\sigma_{t\bar{t}} = 7.04 \pm 0.704$ pb [19], and take the
 445 HF K -factor to be 1.4 ± 0.4 .

446 The fitted b -tag and mistag SFs are shown in Figures 8 and 9, respectively,
 447 as functions of the minimum HOBIT output value. The curves represent
 448 a linear fit to the b -tag SF as a function of the minimum HOBIT output
 449 value, and a parabolic fit to the mistag SF. The variation due to $\sigma_{t\bar{t}}$ is also
 450 shown, where we take the larger of the two shifts in the result due to an
 451 increase/decrease in $\sigma_{t\bar{t}}$ and then symmetrize the uncertainty.

452 The determination of the b -tag and mistag SFs are subject to the same
 453 sources of systematic uncertainty as a measurement of $\sigma_{t\bar{t}}$ [20]. Specifically,
 454 the $t\bar{t}$ acceptance depends on initial-state radiation and final-state radiation
 455 (ISR+FSR), parton distribution functions (PDFs), jet energy scale, trigger
 456 efficiencies and lepton identification efficiencies. The luminosity uncertainty,
 457 although nearly absent in the results of Ref. [20], also contributes to the
 458 overall systematic uncertainty.

459 For the loose (0.72) and tight (0.98) HOBIT operating points, this method
 460 yields efficiency SFs of 0.997 ± 0.037 and 0.917 ± 0.069 , respectively. The
 461 mistag rate SFs are 1.391 ± 0.202 and 1.515 ± 0.291 . A complete table
 462 of systematic uncertainties for the efficiency SF is shown in Table 2, and
 463 for the mistag matrix SF in Table 3. Figures 10, 11, 12, 13, and 14 show
 464 validation plots comparing properties of the highest E_T jet (HOBIT output,
 465 and select HOBIT inputs) in $WH \rightarrow l\nu b\bar{b}$ candidate events before any b -
 466 tag requirements or SF corrections are applied for MC versus data. Good
 467 agreement is seen between MC and data.

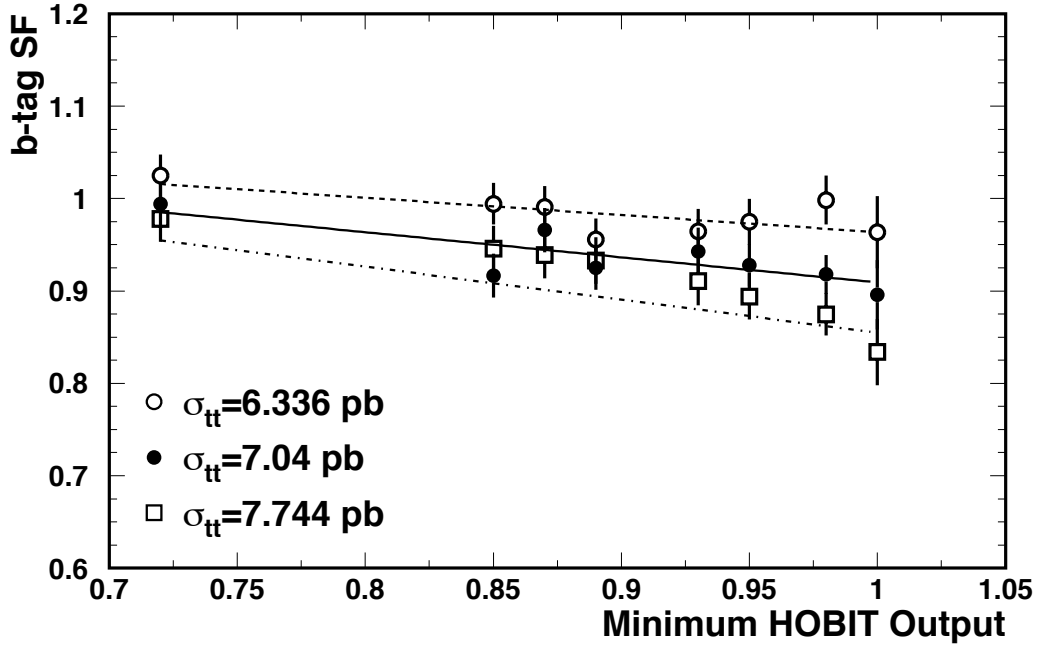


Figure 8: The measured value of the b -tag scale factor for the HOBIT tagger as a function of the minimum HOBIT output value. Variations are shown assuming two values of the $t\bar{t}$ cross section. The straight lines are fits to the SFs assuming the central value of the $t\bar{t}$ cross section, and $\sigma_{t\bar{t}} = 6.336$ pb, the more conservative case for the purpose of estimating uncertainties. The latter fit has been reflected through the central line to obtain a symmetric uncertainty band.

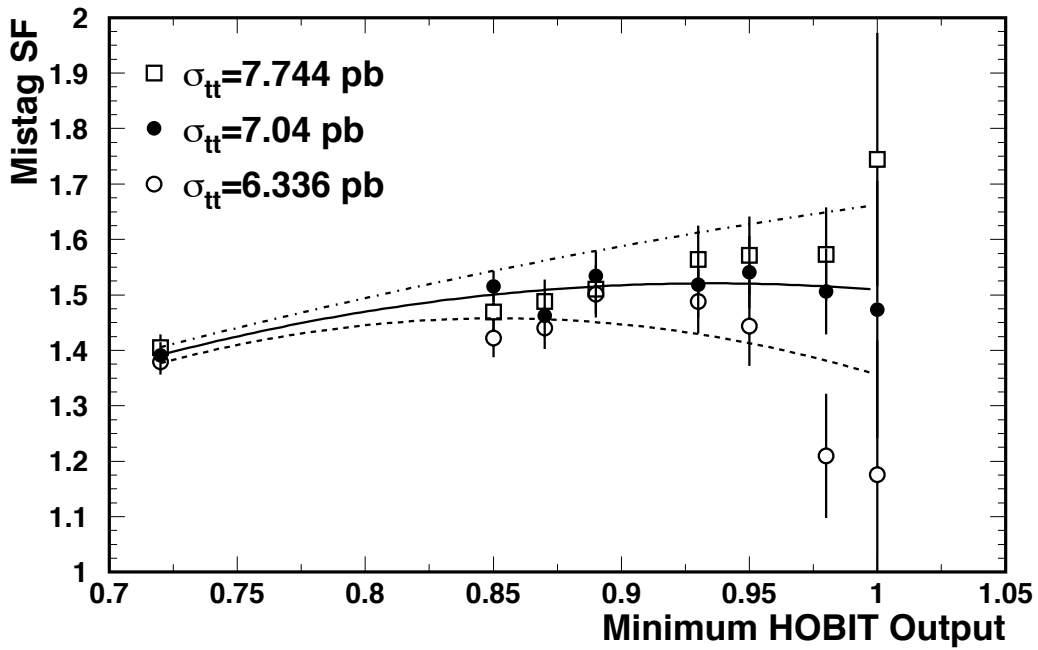


Figure 9: The measured value of the mistag scale factor for the HOBIT tagger as a function of the minimum HOBIT output value. Variations are shown assuming two values of the $t\bar{t}$ cross section. Parabolas are fit to the results assuming the central value of the $t\bar{t}$ cross section, and for $\sigma_{t\bar{t}} = 6.336$ pb. The latter has been reflected through the curve for the central value to obtain the depicted uncertainty band.

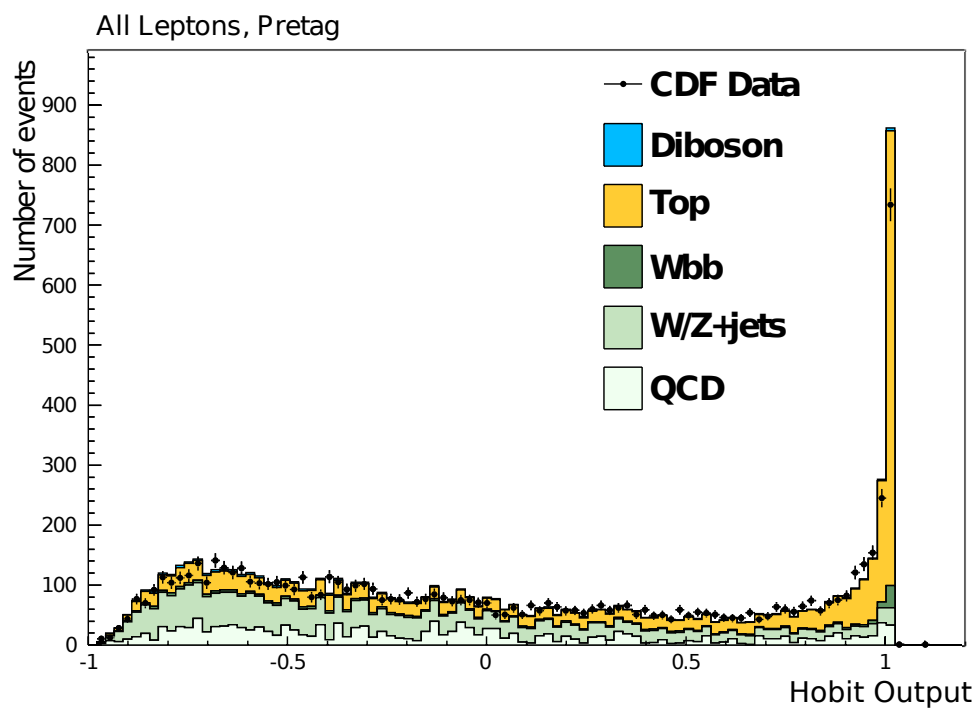


Figure 10: Data versus MC, the HOBIT output distribution of the highest E_T jet from events in the $WH \rightarrow l\nu b\bar{b}$ sample before a requirement of a b -jet tag.

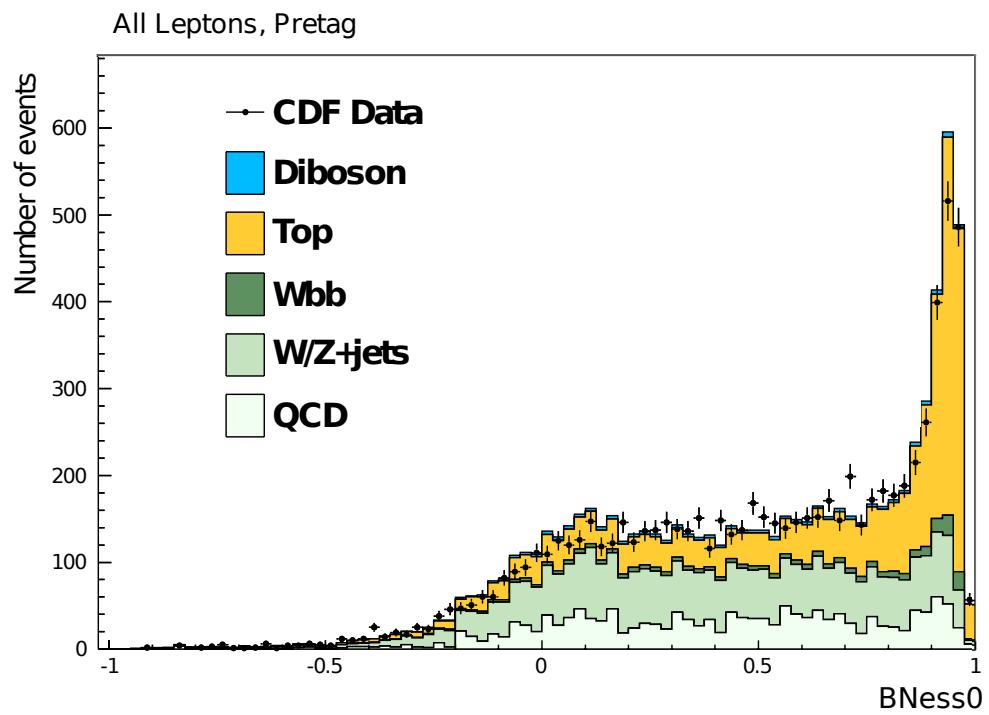


Figure 11: Data versus MC, highest track Bness of the highest E_T jet from events in the $WH \rightarrow l\nu b\bar{b}$ sample before a requirement of a b -jet tag.

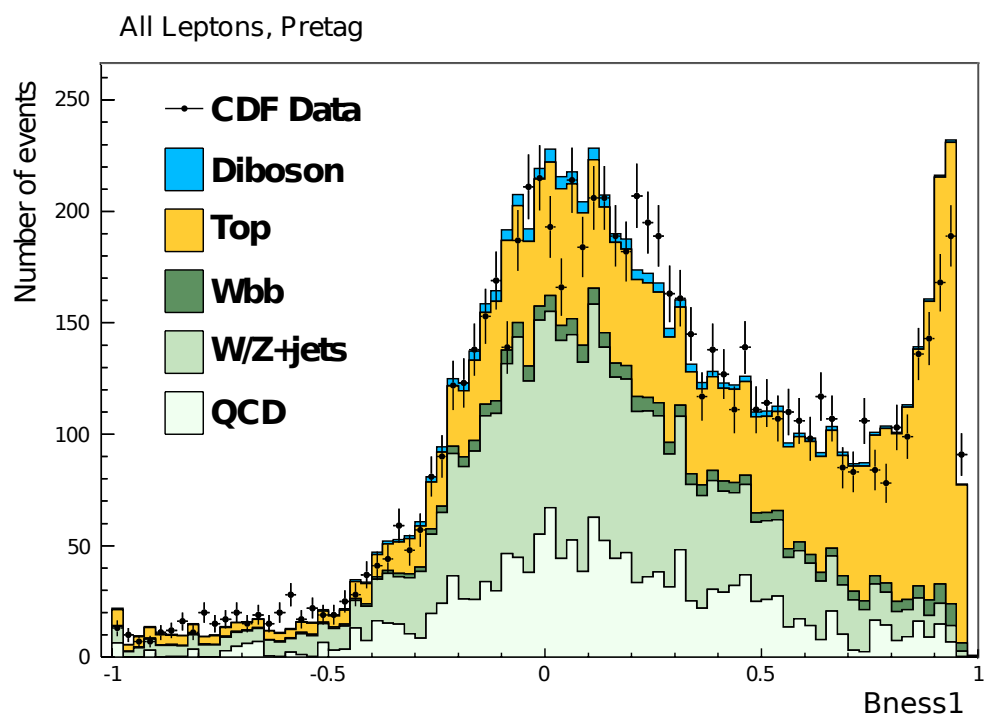


Figure 12: Data versus MC, second highest track B_{ness} of the highest E_T jet from events in the $WH \rightarrow l\nu b\bar{b}$ sample before a requirement of a b -jet tag.

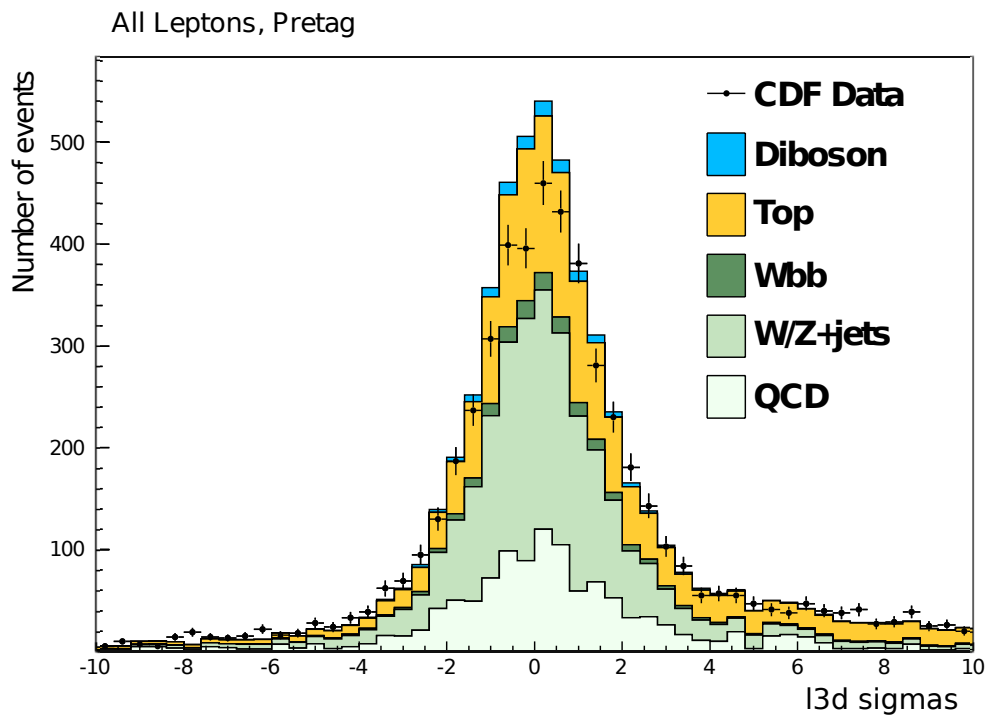


Figure 13: Data versus MC, 3-d displacement significance of most HF-like displaced vertex of the highest E_T jet from events in the $WH \rightarrow l\nu b\bar{b}$ sample before a requirement of a b -jet tag.

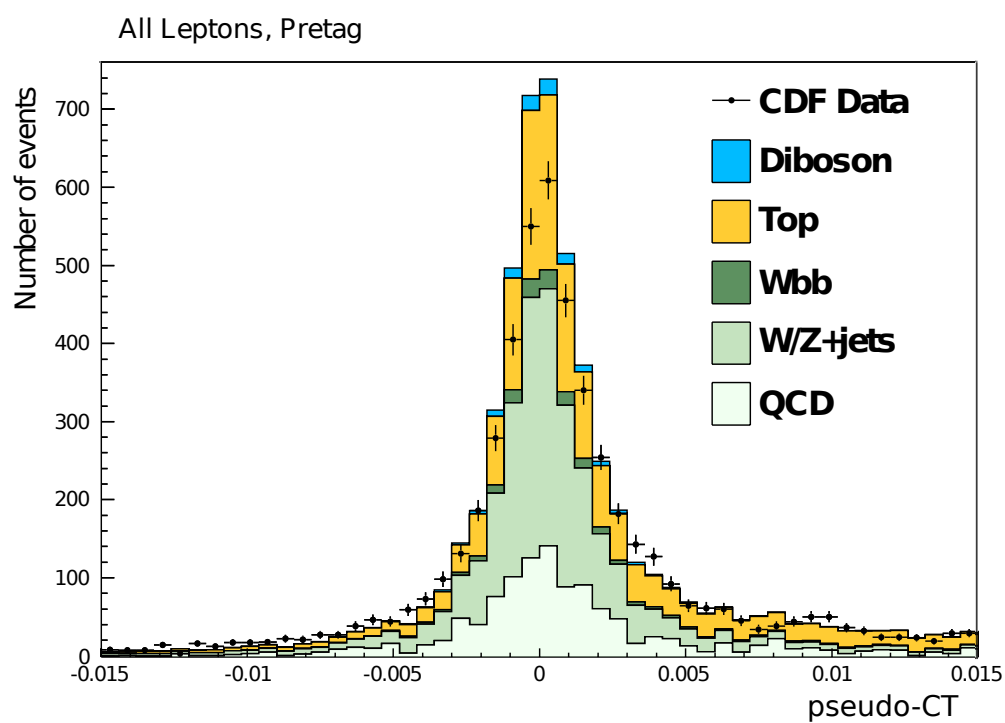


Figure 14: Data versus MC, pseudo- $c\tau$ of most HF-like displaced vertex of the highest E_T jet from events in the $WH \rightarrow l\nu b\bar{b}$ sample before a requirement of a b -jet tag.

468 *6.2. Scale factors using the electron conversion method*

469 A second method of calculating the correction for the HOBIT MC re-
 470 sponse involves a modification of the traditional SecVtx efficiency SF algo-
 471 rithm in a way that does not require the concept of a “negative tag” [16].
 472 However, like the SecVtx technique, this method takes advantage of the HF
 473 enhancement among jets containing electrons, discriminating between HF
 474 and LF jets based upon whether the electron is identified as coming from a
 475 photon conversion.

The event sample consists of back-to-back dijet events where one jet con-
 tains an electron candidate (the electron jet, or “e-jet”), while its opposite
 jet has no such requirement (the away jet, or “a-jet”). We can label each jet
 originating either from an HF quark (“B”) or a light flavor quark or gluon
 (“Q”) and categorize each event as N_{XY} , where the e-jet has flavor X and
 the a-jet has flavor Y. Then the total number of events (N^e) is

$$N^e = N_{BB} + N_{BQ} + N_{QB} + N_{QQ}$$

and the HF fraction of the e-jets is

$$F_B = (N_{BB} + N_{BQ})/N^e.$$

Applying a b tag on the e-jet with a tagging efficiency (ϵ^e) and a mistag rate
 (ϵ_{mis}), the number of b -tagged e-jets (N_+^e) is

$$N_+^e = \epsilon^e \cdot (N_{BB} + N_{BQ}) + \epsilon_{mis}^e \cdot (N_{QB} + N_{QQ}).$$

Assuming the fraction of light flavor jets with conversions is f^c and the
 conversion finding efficiency is ϵ^c for the light flavor jets and ϵ^0 for the HF
 jets, we can obtain the number of e-jets identified from the conversion N^{ec}
 as

$$N^{ec} = \epsilon^0 \cdot (N_{BB} + N_{BQ}) + \epsilon^c \cdot f^c \cdot (N_{QB} + N_{QQ})$$

After tagging, the number of b -tagged conversion e-jets (N_+^{ec}) becomes

$$N_+^{ec} = k \cdot \epsilon^e \cdot \epsilon^0 \cdot (N_{BB} + N_{BQ}) + \epsilon_{mis}^e \cdot \epsilon^c \cdot f^c \cdot (N_{QB} + N_{QQ}),$$

476 where k is the ratio of the b -tag efficiency for an HF e-jet identified as a
 477 conversion to that for one that is not.

The previous two equations allow us to solve for ϵ_{mis} and ϵ^e :

$$\epsilon_{mis} = (N_+^{ec} - k \cdot \epsilon^0 \cdot N_+^e) / (N^{ec} - \epsilon^0 \cdot N^e \cdot (k + (1 - k) \cdot F_B))$$

and

$$\epsilon^e = (N_+^e - \epsilon_{mis} \cdot N^e \cdot (1 - F_B)) / (N^e \cdot F_B).$$

478 Here, all terms that are not the mistag and efficiency rates can be counted
 479 directly in data, taken from MC (k), measured in data (F_B) or both taken
 480 from MC and/or measured in data (ϵ^0). In the case of F_B , we can simply
 481 use the traditional SecVtx electron method [16] to give us this value. For
 482 ϵ^0 , obtaining this quantity from MC is trivial, as we have truth information
 483 available. To calculate it from data, we look at the rate at which positively
 484 SecVtx-tagged jets are found to contain conversion electrons and then adjust
 485 this rate using negatively-SecVtx-tagged jets.

486 The resulting tagging efficiency SFs for the loose and tight HOBIT out-
 487 puts are 0.986 ± 0.066 and 0.949 ± 0.044 respectively, in good agreement
 488 with the results from the $t\bar{t}$ method. Some of the largest contributors to the
 489 systematic component of these uncertainties includes the difference between
 490 the results when we use the MC-calculated ϵ^0 versus the data-calculated ver-
 491 sion and the fact that b -jets containing electrons tend to leave fewer tracks
 492 than typical b -jets.

493 The SFs on the mistag rate for the loose and tight HOBIT operating
 494 points are 1.28 ± 0.17 and 1.42 ± 0.89 , respectively, also consistent with the
 495 results of the $t\bar{t}$ method. As a check, we compare e-jets in data and MC
 496 (Figs. 15 and 16), after purifying the HF content by requiring the away jet
 497 to be tight SecVtx tagged and the electron in the e-jet to not be identified
 498 as a conversion. The fraction of HF versus light jet MC used in these plots
 499 is determined via a fit of MC templates to the HOBIT distribution in data.

500 6.3. SF Combination

501 When combining the correction SFs for the MC b -tag efficiency from the
 502 electron and $t\bar{t}$ method, we obtain 0.993 ± 0.032 (for HOBIT's loose operating
 503 point, 0.72) and 0.937 ± 0.037 (HOBIT's tight operating point, 0.98). The
 504 combined results for the mistag rates are 1.331 ± 0.130 and 1.492 ± 0.277 ,
 505 respectively. Due to the uncertainties in the electron and $t\bar{t}$ methods being
 506 uncorrelated, the combination is straightforward. This results in a greater
 507 than 25% reduction in the size of the uncertainty on the b -tag efficiency
 508 in comparison to the previous most widely used CDF b -tagging algorithm,
 509 SecVtx.

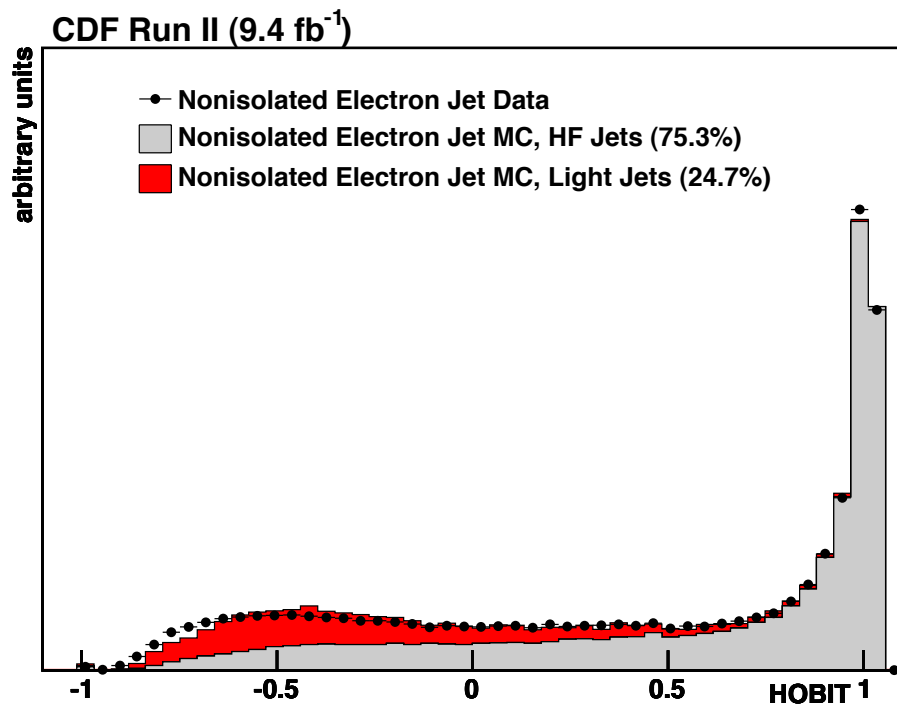


Figure 15: HOBIT output for electron jets, data versus MC. Relative proportions of HF to light jets are determined via a fit of the two MC templates to the data.

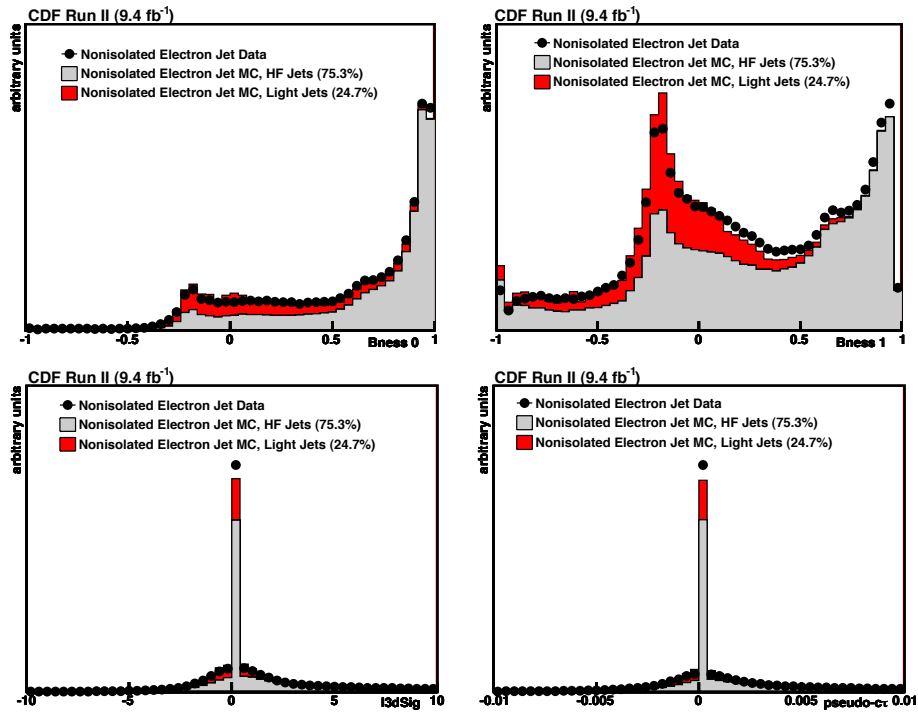


Figure 16: Comparison of select HOBIT inputs for electron jets, data versus MC.

510 **7. Conclusion**

511 We have developed an NN-based b identification tagger which improves
512 upon the best ideas of previous CDF taggers, has a very generous taggability
513 requirement, and has been optimized for $H \rightarrow b\bar{b}$ searches, the primary decay
514 channel of the light Higgs boson at the Tevatron. Using two uncorrelated
515 and innovative methods, we found tagging efficiencies, mistag rates, and
516 data-to-MC scale factors that are in good agreement. The combination of
517 these methods results in a greater than 25% reduction in the b -tag efficiency
518 uncertainty compared to SecVtx, the previous most widely used CDF b -
519 tagging algorithm. In the current light Higgs boson analyses at CDF, we
520 estimate that replacing previous tagging algorithms with HOBIT results in
521 a 10-20% improvement in Higgs boson sensitivity.

522 **Acknowledgements**

523 The authors thank the CDF collaboration, the Fermilab staff and the
524 technical staffs of the participating institutions for their vital contributions.
525 This work was supported by the US Department of Energy and the Fermilab
526 Research Alliance International Fellowship.

- 527 [1] V.M. Abazov, et al., b-Jet Identification in the D0 Experiment, Nucl.
528 Instrum. Methods A 620 (2-3) (2010) 490.
- 529 [2] CMS Collaboration, Performance of the b-jet Identification in CMS,
530 CMS Physics Analysis Summary.
- 531 [3] ATLAS Collaboration, Commissioning of the ATLAS High-Performance
532 b-Tagging Algorithms in the 7 TeV Collision Data, ATLAS CONF Note.
- 533 [4] D. Acosta, et al., Measurement of the $t\bar{t}$ Production Cross Section in $p\bar{p}$
534 Collisions at $\sqrt{s} = 1.96$ TeV Using Lepton+Jets Events with Secondary
535 Vertex b -tagging, Phys. Rev. D 71 (2005) 052003.
- 536 [5] D. Acosta, et al., Measurement of the $t\bar{t}$ Production Cross Section in $p\bar{p}$
537 Collisions at $\sqrt{s} = 1.96$ TeV Using Lepton+Jets Events with Semilep-
538 tonic B Decays to Muons, Phys. Rev. D 72 (2005) 032002.
- 539 [6] C. Ferrazza, Identificazione di quark pesanti in getti adronici in inter-
540 azioni $p\bar{p}$ con il rivelatore CDF al Tevatron, Master's thesis, Universita
541 "La Sapienza" Roma (2006).

- 542 [7] P. Mastrandrea, Study of the heavy flavour fractions in Z+jets events
543 from $p\bar{p}$ collisions at energy = 1.96 TeV with the CDF II detector at the
544 Tevatron collider, FERMILAB-THESIS-2008-63.
- 545 [8] J. Freeman, et al., An Artificial Neural Network Based B -Jet Identifica-
546 tion Algorithm at the CDF Experiment, Nucl. Instrum. Meth. A, Vol.
547 663 (2012), pp. 27-37.
- 548 [9] T. Sjostrand, S. Mrenna, P. Skands, "PYTHIA 6.4 Physics and Manual",
549 arXiv:hep-ph/0603175v2.
- 550 [10] T. Aaltonen, et al., Search for $WZ+ZZ$ Production with Missing Trans-
551 verse Energy+Jets with b Enhancement at $\sqrt{s}=1.96$ TeV, Phys. Rev.
552 D 85 (2012) 012002.
- 553 [11] A. Abulencia, et al., Measurements of inclusive W and Z cross sections
554 in $p\bar{p}$ collisions at $\sqrt{s}=1.96$ TeV, J. Phys. G 34 (2007) 2457.
- 555 [12] T. Affolder, et al., CDF Central Outer Tracker, Nucl. Instrum. Methods
556 A 526 (3) (2004) 249.
- 557 [13] F. Abe, et al., Topology of three-jet events in $p\bar{p}$ collisions at $\sqrt{s}=1.8$
558 TeV, Phys. Rev. D 45 (1992) 1448.
- 559 [14] A. Bhatti, et al., Determination of the jet energy scale at the Collider
560 Detector at Fermilab, Nucl. Instrum Methods A 566 (2) (2006) 375.
- 561 [15] A. Hoecker, P. Speckmayer, J. Stelzer, J. Therhaag, E. von Toerne, and
562 H. Voss, "TMVA: Toolkit for Multivariate Data Analysis," PoS A CAT
563 040 (2007) [physics/0703039].
- 564 [16] Henri Bachacou, A Measurement of the Production Cross Section of $t\bar{t}$
565 Pairs Using Secondary Vertex b -tagging, FERMILAB-THESIS-2004-48.
- 566 [17] D. Acosta, et al., Measurement of the $t\bar{t}$ Production Cross Section in $p\bar{p}$
567 Collisions at $\sqrt{s}=1.96$ TeV Using Lepton+Jets Events with Semileptonic
568 B Decays to Muons, Phys. Rev. D 71, 052003 (2005).
- 569 [18] Nazim Hussain, A simultaneous measurement of the b -tagging efficiency
570 scale factor and the $t\bar{t}$ Production Cross Section at the Collider Detector
571 at Fermilab, FERMILAB-MASTERS-2011-02.

- 572 [19] U. Langenfeld, S. Moch and P. Uwer, Measuring the running top-quark
573 mass, Phys. Rev. D 80, 054009 (2009).
- 574 [20] T. Aaltonen *et al.*, First Measurement of the Ratio $\sigma(tt\bar{t})/\sigma(Z/\gamma^{**} \rightarrow \ell\ell)$
575 and Precise Extraction of the $t\bar{t}$ Cross Section, Phys. Rev. Lett. **105**,
576 012001 (2010).

Jet (HOBIT) Input	Importance
RomaVtx pseudo- $c\tau$	435
RomaVtx 3-d displacement significance	382
Bness 0	77.5
Bness 1	21.5
SecVtx Loose	16.9
Bness 3	9.90
Number of muons	7.80
ptFrac	7.05
Bness 2	6.22
Bness 4	5.46
muon p_T to jet axis	5.32
Bness 5	4.54
Bness 9	4.46
M_{inv} of HF-like tracks	4.17
Bness 6	3.44
Bness 8	2.70
RomaVtx 3-d displacement	2.24
SecVtx Mass	1.68
Bness 7	1.51
RomaVtx Mass	0.752
Number of track-by-track NN tracks	0.380
Number of HF-like tracks	0.287
Jet E_T	0.161
Number of Roma-selected tracks	0.125
Total p_T of tracks	0.00250

Table 1: Inputs to the HOBIT tagger and their importances; ranking is done by importance (see text for definition of this term). “RomaVtx” denotes the most HF-like vertex as found by the RomaNN tagger.

Table 2: The systematic uncertainties for the b -jet tagging efficiency scale factor from the $\sigma(t\bar{t})$ method measurement. This uncertainty must be combined with the electron method scale factor uncertainty; the two should be treated as uncorrelated. The uncertainties shown below are absolute shifts.

b-eff SF $\sigma(t\bar{t})$ method		HOBIT Operating Point	
source		Loose	Tight
$\sigma(t\bar{t})$	up	-0.011	-0.019
	down	0.011	0.019
luminosity	up	-0.004	-0.055
	down	0.007	0.012
jet energy scale	up	-0.005	-0.007
	down	0.005	0.007
generator	up	0.003	0.005
	down	-0.003	-0.005
ISR/FSR	up	-0.001	-0.001
	down	0.001	0.001
$t \rightarrow Wb$ branching ratio	up	-0.001	-0.001
	down	0.001	0.001
Trigger	up	-0.001	-0.001
	down	0.001	0.001
PDF	up	0.001	0.001
	down	-0.001	-0.001
W+j kfactor	up	0.009	0.006
	down	-0.009	-0.006
Statistics	up	0.014	0.008
	down	-0.014	-0.008
total	up	0.022	0.026
	down	-0.022	-0.026

Table 3: The systematic uncertainties for the mistag rate scale factor from the $\sigma(t\bar{t})$ method measurement. This uncertainty must be combined with the electron method scale factor uncertainty; the two should be treated as uncorrelated. The uncertainties shown below are absolute shifts.

mistag SF $\sigma(t\bar{t})$ method		HOBIT Operating Point	
source		Loose	Tight
$\sigma(t\bar{t})$	up	0.007	0.090
	down	-0.007	-0.090
luminosity	up	0.004	0.055
	down	-0.004	-0.055
jet energy scale	up	0.003	0.037
	down	-0.003	-0.037
generator	up	0.002	0.023
	down	-0.002	-0.023
ISR/FSR	up	0.000	0.005
	down	-0.000	-0.005
$t \rightarrow Wb$ branching ratio	up	0.000	0.005
	down	-0.000	-0.005
Trigger	up	0.000	0.005
	down	-0.000	-0.005
PDF	up	0.000	0.005
	down	-0.000	-0.005
W+j kfactor	up	-0.091	-0.135
	down	0.055	0.081
Statistics	up	0.024	0.125
	down	-0.024	-0.125
total	up	0.094	0.217
	down	-0.060	-0.180

Table 4: The systematic uncertainties for the b -jet tagging efficiency scale factor from the electron method measurement. This uncertainty must be combined with the $\sigma(t\bar{t})$ method scale factor uncertainty; the two should be treated as uncorrelated. The uncertainties shown below are absolute shifts.

b-eff SF electron method		HOBIT Operating Point	
source		Loose	Tight
over eff.	up	0.009	0.014
	down	-0.009	-0.014
prescale coor.	up	0.001	0.011
	down	-0.001	-0.011
Et depend.	up	0.010	0.003
	down	-0.010	-0.003
semi-lep bias	up	0.010	0.006
	down	-0.010	-0.006
charm model	up	0.001	0.002
	down	-0.001	-0.002
Stats	up	0.016	0.018
	down	-0.016	-0.018
total	up	0.023	0.026
	down	-0.023	-0.026

Table 5: The systematic uncertainties for the mistag rate scale factor from the electron method measurement. This uncertainty must be combined with the $\sigma(t\bar{t})$ method scale factor uncertainty; the two should be treated as uncorrelated. The uncertainties shown below are absolute shifts.

b-eff SF electron method		HOBIT Operating Point	
source		Loose	Tight
over eff.	up	0.024	0.092
	down	-0.024	-0.092
prescale coor.	up	0.010	0.003
	down	-0.010	-0.003
Et depend.	up	0.014	0.018
	down	-0.014	-0.018
semi-lep bias	up	0.040	0.055
	down	-0.040	-0.055
charm model	up	0.001	0.004
	down	-0.001	-0.004
Stats	up	0.078	0.163
	down	-0.078	-0.163
total	up	0.092	0.196
	down	-0.092	-0.196